Title

Ionization and dissociation dynamics of vinyl bromide probed by femtosecond extreme ultraviolet transient absorption spectroscopy.

Journal

The Journal of chemical physics, 140(6)

ISSN

0021-9606

Authors

Lin, Ming-Fu
Neumark, Daniel M
Gessner, Oliver
et al.

Publication Date

2014-02-01

DOI

10.1063/1.4865128

Peer reviewed

Ionization and dissociation dynamics of vinyl bromide probed by femtosecond extreme ultraviolet transient absorption spectroscopy

Cite as: J. Chem. Phys. **140**, 064311 (2014); https://doi.org/10.1063/1.4865128
Submitted: 30 August 2013 . Accepted: 27 January 2014 . Published Online: 13 February 2014

Ming-Fu Lin, Daniel M. Neumark, Oliver Gessner, and Stephen R. Leone

Ionization and dissociation dynamics of vinyl bromide probed by femtosecond extreme ultraviolet transient absorption spectroscopy

Ming-Fu Lin,[1,2] Daniel M. Neumark,[1,2] Oliver Gessner,[1] and Stephen R. Leone[1,2,3]
[1]*Ultrafast X-ray Science Laboratory, Chemical Sciences Division, Lawrence Berkeley National Laboratory, Berkeley, California 94720, USA*
[2]*Department of Chemistry, University of California, Berkeley, California 94720, USA*
[3]*Department of Physics, University of California, Berkeley, California 94720, USA*

(Received 30 August 2013; accepted 27 January 2014; published online 13 February 2014)

Strong-field induced ionization and dissociation dynamics of vinyl bromide, CH_2=CHBr, are probed using femtosecond extreme ultraviolet (XUV) transient absorption spectroscopy. Strong-field ionization is initiated with an intense femtosecond, near infrared (NIR, 775 nm) laser field. Femtosecond XUV pulses covering the photon energy range of 50-72 eV probe the subsequent dynamics by measuring the time-dependent spectroscopic features associated with transitions of the Br (3*d*) inner-shell electrons to vacancies in molecular and atomic valence orbitals. Spectral signatures are observed for the depletion of neutral C_2H_3Br, the formation of $C_2H_3Br^+$ ions in their ground ($\tilde{X}$) and first excited ($\tilde{A}$) states, the production of $C_2H_3Br^{++}$ ions, and the appearance of neutral Br ($^2P_{3/2}$) atoms by dissociative ionization. The formation of free Br ($^2P_{3/2}$) atoms occurs on a timescale of 330 ± 150 fs. The ionic $\tilde{A}$ state exhibits a time-dependent XUV absorption energy shift of ∼0.4 eV within the time window of the atomic Br formation. The yield of Br atoms correlates with the yield of parent ions in the $\tilde{A}$ state as a function of NIR peak intensity. The observations suggest that a fraction of vibrationally excited $C_2H_3Br^+$ ($\tilde{A}$) ions undergoes intramolecular vibrational energy redistribution followed by the C–Br bond dissociation. The $C_2H_3Br^+$ ($\tilde{X}$) products and the majority of the $C_2H_3Br^{++}$ ions are relatively stable due to a deeper potential well and a high dissociation barrier, respectively. The results offer powerful new insights about orbital-specific electronic processes in high field ionization, coupled vibrational relaxation and dissociation dynamics, and the correlation of valence hole-state location and dissociation in polyatomic molecules, all probed simultaneously by ultrafast table-top XUV spectroscopy. © *2014 AIP Publishing LLC*. [http://dx.doi.org/10.1063/1.4865128]

I. INTRODUCTION

Static extreme ultraviolet (XUV) and X-ray absorption spectroscopy has been widely applied to studies of polyatomic molecules in gas, liquid, and surface environments.[1–5] Core-to-valence transitions can be used to selectively probe the chemical composition, oxidation states, valence orbital symmetries, and alignment of molecules. With the development of time-resolved methods utilizing XUV and X-ray light sources,[6–23] investigations using core-to-valence transitions can be extended to the time domain. Ultrafast dynamics in the vicinity of specific chemical elements and reaction centers within transient molecular species can now be monitored in real-time.[9–13,24,25] Ultrafast electronic motion and structural relaxation can be explored with atomic site specificity.[26–30] Recently, table-top high harmonic sources with attosecond and femtosecond time resolution have been employed to investigate ultrafast physics and chemistry of helium, neon, argon, krypton, xenon, CH_2Br_2, and Br_2.[26,31–43] The new generation of laboratory-based experiments enables the real-time probing of ultrafast electronic wavepackets,[26] vibrational wavepackets,[43] and dissociative ionization (DI)[34] of polyatomic molecules prepared by coherent strong-field laser ionization.

Strong-field ionization (SFI) of polyatomic molecules accesses multiple electronic continua corresponding to different ionized molecular valence orbitals,[44–46] i.e., the ionization process simultaneously generates ions in several electronic states, some of which may dissociate. However, the relation between the molecular fragments and the parent ionic states is rarely explored in SFI. The multielectron response of an atom or molecule to a nonresonant strong field leads to complex ionization mechanisms. For example, nonadiabatic multielectron (NME) excitation[44,46,47] can generate ions preferentially in electronically excited states and can greatly affect the molecular dissociation pathways.[47,48] SFI-induced relaxation and dissociation dynamics in polyatomic molecules are often difficult to trace in experiments that detect only the asymptotic dissociation products with techniques such as time-of-flight (TOF) mass spectrometry. A recently developed technique that detects both ions and electrons in coincidence has been able to correlate fragment ions with distinct, initially excited parent ion states.[43] Pump-probe techniques with a state-resolving capability such as the transient absorption method are particularly valuable to obtain the lifetimes of dissociative ions.

Here, femtosecond time-resolved XUV (50 eV–72 eV) transient absorption measurements are performed on vinyl bromide molecules (CH_2=CHBr) that are ionized by an intense NIR laser field (∼10^{14} W/cm^2, λ = 775 nm). The experiment focuses on the study of strong-field produced molecular ions and their relaxation dynamics. The detailed mechanism

of the ionization process itself (e.g., tunneling versus multiphoton ionization) cannot be explored in this study since the experiment is not sensitive to the intricate molecular dynamics that take place during the presence of the strong NIR field. The strong NIR field can ionize electrons from several occupied molecular orbitals, producing a variety of ionic states. The resulting valence hole configurations are probed by XUV light that promotes electrons from the Br ($3d$) inner-shell to partly filled valence orbitals at transition energies between 64 eV and 69 eV corresponding to the $M_{4/5}$ edge. Assignment of the major spectral features indicates that the transient XUV absorption spectrum directly monitors and distinguishes among parent ions with HOMO and HOMO−1 valence holes, atomic Br fragments, and doubly charged ions, all of which are generated by the NIR pulse.

From the spectroscopic assignments, we rationalize the formation and dissociation dynamics of strong-field induced vinyl bromide ions ($C_2H_3Br^+$) in the electronic ground ($\tilde{X}$) and first excited ($\tilde{A}$) state. Formation of $C_2H_3Br^{++}$ dications is also observed. An ultrafast transient XUV absorption energy shift in the singly charged ionic $\tilde{A}$ state is observed, suggesting a possible correlation with the C–Br bond dissociation that produces free atomic Br ($^2P_{3/2}$). In contrast, ions in the ionic $\tilde{X}$ ground state and doubly charged ions ($C_2H_3Br^{++}$) appear to be more stable. Electronic structure calculations are performed to elucidate the stability of doubly charged ions. The results offer new insights into the temporal evolution of parent ions in different ionic states and their correlation to emerging molecular fragments.

II. EXPERIMENTAL AND THEORETICAL METHODS

A schematic of the tabletop XUV transient absorption setup is shown in Fig. 1. A detailed description of the experiment is provided in Ref. 33. Briefly, a high power NIR femtosecond laser system provides pulses with a center wavelength of 775 nm. The M^2 value and beam diameter ($1/e^2$) of laser system are ∼1.5 and ∼10 mm, respectively. A 50/50 beam splitter is used to divide the initial NIR energy into a "pump beam" for NIR strong-field ionization and a "probe beam" for high harmonic generation (HHG). Both beams are combined in a 10 mm long absorption cell that is filled with 0.27 kPa of vinyl bromide. The NIR pump beam is focused by an f/40 spherical lens of effective focal distance of ∼1 m. The XUV probe beam is focused by a toroidal mirror.[33] The XUV and NIR beam diameters ($1/e^2$) at the focus (i.e., target cell position) are 100 ± 10 μm and 150 ± 10 μm, respectively, both measured by using knife-edge scans. The XUV beam diameter is two-thirds of the NIR pump beam, which reduces spatial averaging effects in the detected ionic states due to the NIR intensity profile. In the pump-probe experiment, a positive time delay indicates that the NIR pump pulse arrives at the sample before the XUV probe pulse. All experiments are performed with parallel pump and probe beam polarizations.

A calibrated power meter, placed in front of the vacuum entrance window, is used to measure the NIR power for the pump beam. The pulse duration is measured by using an interferometric autocorrelator. The estimated peak intensity of the NIR pump beam for strong-field ionization ranges from

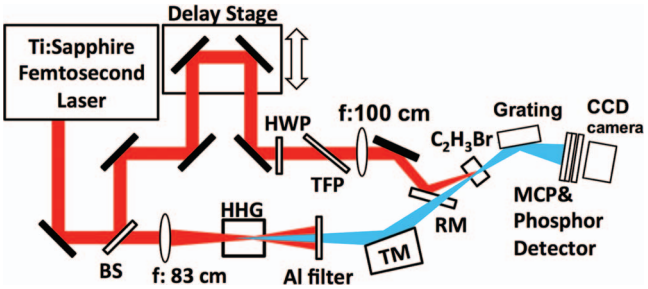

FIG. 1. Experimental setup for XUV transient absorption spectroscopy. The red and blue color lines represent the NIR (pump) and XUV (probe) beams, respectively. The relative delay time is controlled by a delay stage. BS: beam splitter, HHG: high harmonic generation, TM: toroidal mirror, HWP: half wave plate, TFP: thin film polarizer, RM: recombination mirror and MCPs: microchannel plates.

140 (±70) TW/cm^2 to 290 (±100) TW/cm^2. Note that the intensity profile of the NIR beam and the longitudinal extent of the focal volume result in a broad distribution of power densities; the peak intensities are quoted. The XUV probe beam is generated in a 25 mm long gas cell filled with neon gas at a pressure of 3.3 kPa.[17] The generated XUV light with energies between 50 eV and 72 eV has an overall flux of ∼10^5 photons/pulse at the sample cell. Energy calibration of the spectrometer is performed using the characteristic XUV absorption lines of laser-produced Xe^+ ions at transition energies of 55.4 eV and 71 eV.[49–51] A combination of a half-wave plate and a thin film polarizer is used to vary the power of the NIR pump beam.

All transient absorption spectra (delta optical density ΔOD) presented here are obtained by using a transmission spectrum collected at a time delay of −550 fs as a reference.[8,33] The transient optical density is defined as $\Delta OD(E,t) = \log [I(E, t = -550\ fs)/I(E, t)]$, where I(E,t) represents the transmitted intensity at pump-probe time delay t and XUV photon energy E. A small time-independent background from scattered NIR pump photons precludes the use of the pump-off transmission spectra as a reference. Using the transmission spectrum at −550 fs as a reference virtually eliminates the impact of the unavoidable small NIR background that occurs in each transient absorption spectrum. The sample gas pressure in the pump-probe experiments is kept low to prevent clogging of the sample cell resulting in a typical $\Delta OD \leq 0.1$. The spectrum for each time delay is averaged over ten repeated scans resulting in a total data acquisition time of 250 s per delay, yielding a signal-to-noise ratio of ∼5 after ∼10^6 pump-probe pulses. The pulse-to-pulse fluctuations of the XUV photon intensity are the major source of noise in the experiments. Error bars presented in the figures represent 95% confidence intervals derived by statistical analysis of the repeated scans.

Quantum chemistry calculations were carried out for doubly charged $C_2H_3Br^{++}$ ions. Density functional theory (DFT) calculations are performed using the GAUSSIAN 09 program package.[52] The hybrid functions of Becke, 3-parameter, Lee-Yang-Parr (B3LYP) for exchange-correlation energies with the 6-311++G($3d$,$2p$) basis set are employed in the calculations. The calculations yield vertical ionization

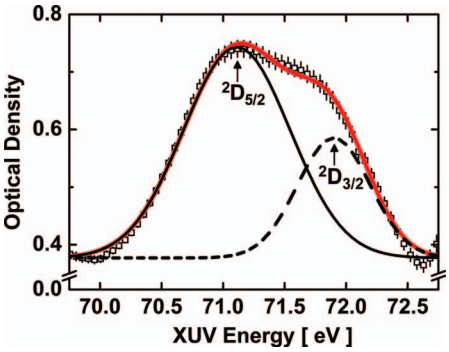

FIG. 2. The static absorption spectrum of neutral vinyl bromide. The transitions correspond to the excitation of Br (3*d*) electrons to the LUMO+1. Experimental result is shown in black open squares with the error bars. Red solid line represents the overall fitting. The features are fit to two Gaussian functions with fixed centers at 71.1 eV and 71.9 eV. The resulting FWHMs are equal to 1.0 eV and 0.7 eV, respectively.

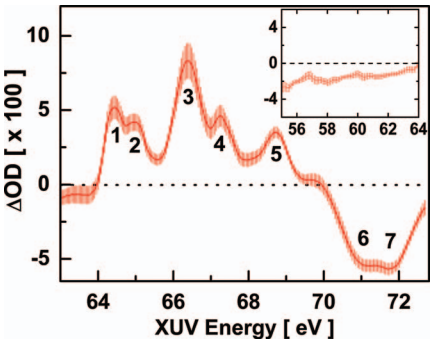

FIG. 3. Transient absorption spectrum at +5 ps. The transient peaks are marked with numbers from 1 to 7. The peaks 6 and 7 represent the neutral vinyl bromide depletion as shown in Fig. 2. The inset shows the next section of depleted non-resonant continuum below 64 eV. The vertical bars represent the statistical 95% confidence interval.

energies (IEs) for the transition from the ground state of C_2H_3Br to $C_2H_3Br^{++}$ ions. The results are tested by comparing calculations for other organic molecules (e.g., ethene, 2-butene, and benzene) with available experimental results.[53] The agreement is within 0.6 eV, verifying the accuracy of the calculations for single and double ionization energies. In addition, the transition state for the dissociation of $C_2H_3Br^{++}$ into $C_2H_3^+ + Br^+$ is characterized. All reported results from this calculation (Sec. V B) include corrections for zero point energy.

III. RESULTS

A. Static and transient absorption spectra

Figure 2 shows a static absorption spectrum of neutral vinyl bromide. The absorption spectrum is obtained from two XUV transmission spectra with and without the gas sample in the target cell. The conversion from transmission to absorption spectra is performed according to OD $= -\log [I(E)/I_0(E)]$, where I (E) and I_0 (E) represent the XUV transmission spectrum with and without vinyl bromide in the sample cell, respectively. The open squares and red solid line represent the experimental data and overall fit result, respectively. The spectrum is fit to two Gaussian features centered at 71.1 eV and 71.9 eV that have been previously assigned to the spin-orbit split transitions from Br (3*d*) inner-shell orbitals to the LUMO+1 orbital (σ^*, C–Br antibonding).[54]

Figure 3 shows a transient absorption spectrum at a pump-probe delay of +5 ps. The ΔOD scale on the vertical axis is proportional to the concentration of transient species in the pump-probe interaction volume. Positive and negative values of ΔOD in Fig. 3 represent the production of transient species and the depletion of ground state neutral molecules, respectively. Several distinct features are seen and marked with numbers from 1 to 7. Negative ΔODs for peaks 6 and 7 correspond to the reduction of resonant absorption according to Fig. 2, i.e., a depletion of the neutral parent molecule. The inset in Fig. 3 shows the extension of a broad, featureless depletion signal at energies below 64 eV. The assignments of peaks 1-5 and further data analysis for Figs. 2 and 3 are presented in Sec. IV A.

Figure 4 shows a two-dimensional false color map of the transient absorption spectra (ΔOD) versus time delay at a NIR peak intensity of 220 ± 90 TW/cm^2. The transient species are labeled according to the peaks shown in Fig. 3. In Fig. 4, the formation of peaks 2 to 5 (yellow/red) and the depletion of peaks 6 and 7 (blue) occur promptly. The rise time of the leading edge of these signals reflects the temporal resolution (instrument response function, IRF ∼61 ± 11 fs) of the experiments. However, peak 1 exhibits a slower rise time of 330 ± 150 fs. Moreover, the absorption maximum of peak 2 evolves from 65.5 eV to 65.1 eV within the rise time of peak 1. This shifting implies that some ultrafast dynamics are imprinted in the time-dependent XUV absorption profile. The transition energies for all other peaks remain constant for all pump-probe delays. Further analysis of Fig. 4 will be presented in Sec. IV A.

B. Power dependence measurements

Figure 5 shows transient spectra taken at 10 ps pump-probe time delay at three different NIR peak intensities

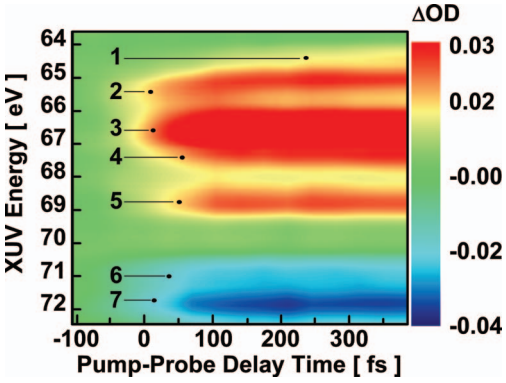

FIG. 4. Two-dimensional false colormap of transient absorption spectrum versus the XUV energy and the pump-probe delay time. The colorbar represents the ΔOD scale. The ΔOD scale is linearly proportional to the intensity of transient species in the pump-probe interaction volume. The transient ions and fragments are labeled according to Fig. 3. Note that the absorption energy of peak 2 evolves from 65.5 eV to 65.1 eV in this pump-probe time window. For other transient species, the absorption energies remain constant.

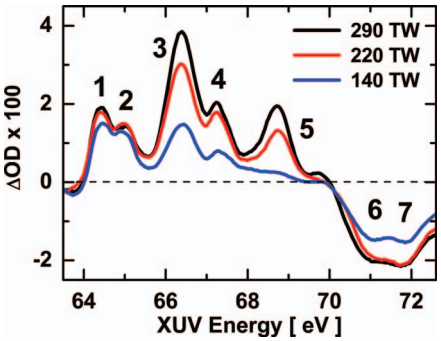

FIG. 5. Power dependence measurements over three different NIR peak intensities at the pump-probe delay time +10 ps. The transient species are labeled accordingly as described in Fig. 3. Some intensity correlations in the transient species are observed.

ranging from 140 ± 70 TW/cm^2 to 290 ± 100 TW/cm^2. The vertical and horizontal axes represent the densities of the transient species and the XUV energies, respectively. The spectra are displayed as recorded with varying NIR intensities and constant XUV intensities; they are not normalized to one another. In the spectra, the amplitudes of peak 1 and peak 2 hardly change with the NIR peak intensity. However, a strong dependence of peaks 3, 4, and 5 on the NIR peak intensity is observed. The depletion of neutral C_2H_3Br at peaks 6 and 7 increases markedly when going from 140 TW/cm^2 to 220 TW/cm^2, but remains virtually constant upon further increase of the peak intensity to 290 TW/cm^2.

C. Calculated molecular orbitals of the vinyl bromide molecule

Figure 6 shows the calculated molecular orbitals (MO) of neutral vinyl bromide using the theoretical methods described in Sec. II. The lowest-lying empty molecular orbitals are the LUMO (lowest unoccupied MO) and LUMO+1 (2nd lowest unoccupied MO), as shown in Figs. 6(a) and 6(b), respectively. The electron density located on the bromine atom is very small in the LUMO. In contrast, the LUMO+1 has significant density on the bromine atom and antibonding character along the C–Br bond. Figure 6(c) shows the HOMO, which has π bonding character between two carbon atoms and π^* antibonding character between the carbon and bromine atoms.[55–58] The electron densities are located above and below the molecular plane, and the wavefunctions have opposite signs around the C–C bond and the bromine atom. The HOMO−1 in Fig. 6(d) has a lone pair of electrons localized on the bromine atom with maximum density in the molecular plane.[55–58] The HOMO−2, shown in Fig. 6(e), has strongly delocalized electron density above and below the molecular plane.

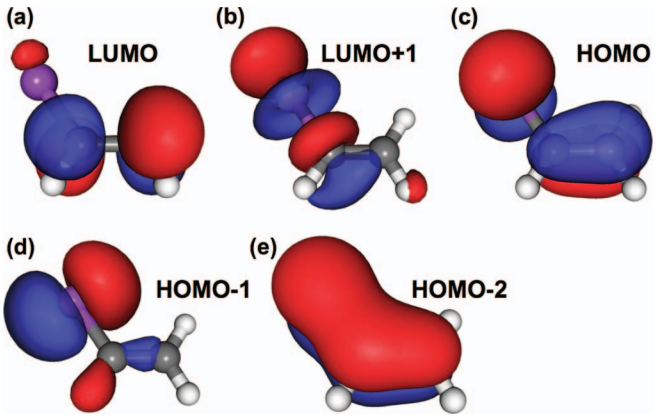

FIG. 6. The molecular orbitals of neutral vinyl bromide calculated using GAUSSIAN 09 program package. (a) LUMO orbital. This orbital possesses an electron density mainly localized on carbon atoms. The electron density on the bromine atom is small. (b) LUMO+1 orbital. It possesses a σ^* antibonding along the C–Br bond. (c) HOMO orbital. The π bonding is between two carbon atoms and the π^* antibonding is between the carbon and bromine atoms, (d) HOMO−1 orbital. This corresponds to p shell lone-pair electrons on the bromine atom in the molecular plane. (e) HOMO−2 orbital. The orbital shows a delocalized electron distribution over the whole molecule.

IV. DATA ANALYSIS

A. Spectroscopic assignments of static and transient absorption spectra

Neutral vinyl bromide has previously been studied using inner-shell electron energy loss spectroscopy (ISEELS) in the vicinity of the Br (3d) absorption edge.[54] The static absorption spectrum in Fig. 2 is analyzed by a fit to two Gaussian peaks (solid and dashed curves). The resulting peak centers are located at 71.1 eV and 71.9 eV, respectively. The obtained full widths at half maximum (FHWM) are 1.0 eV and 0.7 eV. The lower energy component is broader than the higher energy component due to the ligand-field splitting (molecular field splitting) of the Br (3d) inner-shell hole state.[59] The valence spin-orbit splitting of LUMO+1 is of the order of ∼0.05 eV.[60] Vibrational progressions also contribute to the broadening of each absorption peak in the Br (3d)-to-LUMO+1 transition. Note that the static absorption lines in Fig. 2 are not assigned to Br (3d)-to-LUMO transitions as a consequence of negligible spatial overlap between the initial and final molecular orbitals, resulting in negligible oscillator strengths for the corresponding transitions.[54,61] The LUMO has little electron density in the vicinity of the bromine atom (Fig. 6(a)), and thus the Br (3d)-to-LUMO transition probability is very small.

The transient spectrum shown in Fig. 3 is simultaneously fit with multiple Gaussian peaks. The fit results (solid and dashed curves) and assignments are shown in Fig. 7. The peaks represent inner-shell to valence transitions in atomic Br ($^2P_{3/2}$), singly charged parent ions ($C_2H_3Br^+$) in the $\tilde{X}$ and $\tilde{A}$ states, the doubly charged ($C_2H_3Br^{++}$) parent ions, and neutral vinyl bromide. Each feature comprises a pair of inner-shell excited spin-orbit states representing the $3d^{-1}{}_{5/2}$ ($^2D_{5/2}$) and $3d^{-1}{}_{3/2}$ ($^2D_{3/2}$) configurations separated by ∼0.9 eV. The initial values for the peak positions are set according to direct measurements, when available, and estimates. The inner-shell absorption energies of atomic Br (3d) and $C_2H_3Br^{++}$ dications are obtained from the literature.[34,62] The absorption energies of neutral vinyl bromide are obtained from the experimental free fit result shown in Fig. 2. The absorption energies of singly charged parent ions are estimated as illustrated in Fig. 8. The positions, widths, and intensities of all

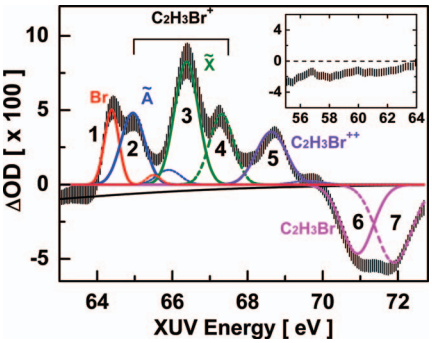

FIG. 7. Transient absorption spectrum at +5 ps. Solid and dashed color lines represent the transient species in different inner-shell spin-orbit states. In the spectrum, the atomic Br ($^2P_{3/2}$), singly charged ionic $\tilde{A}$ state, ionic $\tilde{X}$ state, and doubly charged $C_2H_3Br^{++}$ ions are shown. The depletions of the neutral vinyl bromide at resonance (solid/dashed magenta lines) and non-resonant continuum (black solid line) are considered in the spectra as well. The inset shows the next section of depleted non-resonant continuum below 64 eV.

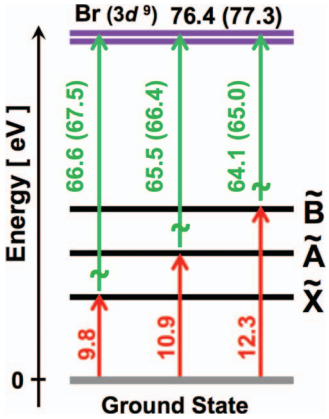

FIG. 8. Predicted inner-shell absorption energies for the Br (3*d*)-to-valence transitions. The energies at 66.6 eV and 67.5 eV represent the transition of two inner-shell excited spin-orbit series of configurations $3d^9$ with term symbols of $^2D_{5/2}$ and $^2D_{3/2}$, respectively. The red arrows represent the ionization of electrons from the HOMO, HOMO−1, and HOMO−2 to the ionization continuum that generates the ionic $\tilde{X}$, $\tilde{A}$, and $\tilde{B}$ states. Green arrows represent the excitation of the ionic states to the inner-shell excited state by promoting a Br (3*d*) electron to the valence holes.

peaks shown in Fig. 7 are allowed to vary simultaneously. The boundary conditions imposed on the fit are that each inner-shell spin-orbit pair has the same width (limited by the experimental energy resolution), and all spin-orbit pairs have the same energy splitting of 0.9 eV. The fit results and initial estimates are listed in Table I.

There are no experimental values available for the Br (3*d*) inner-shell absorption energies of $C_2H_3Br^+$ parent ions in the ionic $\tilde{X}$ and $\tilde{A}$ states. These two ionic states correspond to the ionization of electrons from the HOMO and HOMO−1 orbitals, respectively. The inner-shell to valence level transition energies within the two ionic states are estimated by the difference between the binding energies of Br (3*d*) inner-shell electrons and the IEs of the HOMO and HOMO−1 valence electrons (Fig. 8). The previously measured inner-shell electron binding energies for vinyl bromide are 76.4 ± 0.3 eV and 77.3 ± 0.3 eV for the spin-orbit-split inner-shell states $3d^{-1}{}_{5/2}(^2D_{5/2})$ and $3d^{-1}{}_{3/2}(^2D_{3/2})$, respectively.[34,54,59] The IE of electrons in the HOMO is 9.8 eV.[55–58] Within a simple Koopmans' picture (Fig. 8),[63,64] Br (3*d*)-to-HOMO transition energies of 66.6 ± 0.3 eV and 67.5 ± 0.3 eV are obtained. These values support the assignment of the absorption peaks 3 and 4 (Fig. 7) at 66.4 eV and 67.3 eV to the Br (3*d*)-to-HOMO transitions in the parent $C_2H_3Br^+$ ion.

Following the same procedure as for the HOMO vacancies, the Br (3*d*)-to-HOMO−1 and Br (3*d*)-to-HOMO−2 energies are derived as the difference between the Br (3*d*) ionization energies noted above and previously determined inner valence ionization energies. From VUV experiments on neutral vinyl bromide,[55–58] the IEs of valence electrons in the HOMO−1 and HOMO−2 are 10.9 eV and 12.3 eV, respectively, as indicated by the red arrows in Fig. 8. This yields inner-shell absorption energy estimates of 65.5 ± 0.3 eV/66.4 ± 0.3 eV for the Br (3*d*)-to-HOMO−1 transitions (ionic $\tilde{A}$ state) and 64.1 ± 0.3 eV/65.0 ± 0.3 eV for the Br (3*d*)-to-HOMO−2 transitions (ionic $\tilde{B}$ state). These estimates match well with the fit peaks at 65.1 and 66.0 eV in Table I, so it is reasonable to assign those peaks to the ionic $\tilde{A}$ state. As shown in Figs. 3 and 4, the lack of any clear time-dependent absorption peak centered at 64.1 eV indicates that signal from ions in the $\tilde{B}$ state (i.e., HOMO−2 hole), if present, would appear below our detection limit ($\sim\Delta OD = 0.01$). In addition, the power dependence measurement in Fig. 5 shows no apparent profile change near the overlap between the $\tilde{B}$ state and the atomic Br (peak 1), which might be expected since production of $\tilde{B}$ state ions requires more IR photons. This evidence suggests that we generate the $\tilde{X}$ and $\tilde{A}$ states of the parent ion, but not the $\tilde{B}$ state. From the fit results shown in Fig. 7, the absorption ratios of the inner-shell-excited spin-orbit component ($3d_{5/2}/3d_{3/2}$) for the ionic $\tilde{X}$ and $\tilde{A}$ states are 1.7 ± 0.1 and 2.7 ± 0.2, respectively.

No experimental values are available for the Br (3*d*) inner-shell absorption energies of $C_2H_3Br^{++}$ ions. The

TABLE I. The peak positions/widths (FWHM) from the fits in Fig. 7 (+5 ps) and from the estimates in Fig. 8. The unit is in electron volt (eV).

	Peak position from the fits (eV)	Peak position from the estimates/literature (eV)	Peak width from the fit (eV)
$\tilde{X}$	66.4/67.3	66.6/67.5 (±0.3)	0.75
$\tilde{A}$	65.1/66.0	65.5/66.4 (±0.3)	0.74
$\tilde{B}$	NA	64.1/65 (±0.3)	NA
Br ($^2P_{3/2}$)	64.4/65.4	64.4/65.4	0.45
$C_2H_3Br^{++}$	68.7/69.6	68.9/69.9	0.94

absorption peaks in the spectral range between 68 eV and 70 eV have previously been assigned to doubly charged ground state $CH_2Br_2^{++}$ and Br^{++} ions.[34,62] Thus, the absorption peak in this energy region is assigned to the dication.

The fit results indicate that the ratio of the absorption strengths for the 64.4 eV ($^2P_{3/2} \rightarrow {}^2D_{5/2}$) and 65.4 eV ($^2P_{3/2} \rightarrow {}^2D_{3/2}$) transitions in atomic Br is equal to 5. This value is consistent with the literature.[65] An experimental energy resolution (FWHM) of ∼0.45 eV is derived by deconvoluting the atomic Br (3*d*) line at 64.4 eV, taking into account the natural linewidth (∼0.1 eV).[62] There is no clear evidence for atomic Br production in the valence excited spin-orbit state ($^2P_{1/2}$) from $C_2H_3Br^+$ ions.[66] This result is similar to the results of photoelectron-photoion coincidence experiments, which showed that vinyl bromide parent ions with sufficient energy to dissociate yielded only $C_2H_3{}^+$+Br ($^2P_{3/2}$) products.[67,68]

B. Ultrafast dissociation and relaxation dynamics of $C_2H_3Br^+$ and $C_2H_3Br^{++}$ ions

The time-dependent absorption spectra (such as those shown in Fig. 4) are further analyzed and converted to pump-probe traces as shown in Figs. 9–11. For each transient spectrum corresponding to a specific pump-probe delay, a separate multi-parameter fit is performed as described in Sec. IV A (Fig. 7). This series fits at different delays include a boundary condition that imposes fixed relative absorption strength for each inner-shell spin-orbit pair from Fig. 7. Performing the same fit procedure for multiple time-delays results in the time-dependent signal intensities shown in Figs. 9 and 10 and the peak positions shown in Fig. 11. The careful step-by-step fit procedure is applied in order to separate contributions from overlapping signals in a more reproducible manner than, for example, in a global 2D fit procedure. The latter would also make it more difficult to distinguish between a single signal with a time-dependent energy (such as the $\tilde{A}$ state signal) and several adjacent signals with constant energies but time-dependent intensities. Variations in the peak positions and widths derived by the fit procedure are within 50 meV, except for the ∼0.4 eV shift of the $\tilde{A}$ state energy, confirming the visual identification of the change in the absorption energy near peak 2 in Fig. 4. Figures 9(a)–9(c) show pump-probe traces for the production of singly charged ions in the $\tilde{X}$ state (black), the depletion of neutral vinyl bromide (blue), and the emergence of doubly charged ions (red) over time delays ranging from −0.6 ps to 2.5 ps. Figures 9(d) and 9(e) display pump-probe traces for the emergence of atomic Br ($^2P_{3/2}$) and singly charged ions in the $\tilde{A}$ state, respectively. Figure 10 shows the pump-probe traces for all transient species over time delays ranging from −5 ps to 20 ps, using coarser time intervals.

Figure 9(a) shows that the singly charged ions in the $\tilde{X}$ state (HOMO hole) are produced promptly by the strong laser field. The time constant of the rising edge in Fig. 9(a) is obtained by fitting the data with an error function with a FWHM of 65 ± 14 fs (black line). The depletion of neutral molecules shown in Fig. 9(b) occurs promptly, too, and can be described by an error function with a FWHM of 55 ± 17 fs (blue line). We take the weighted average of these values to be the instru-

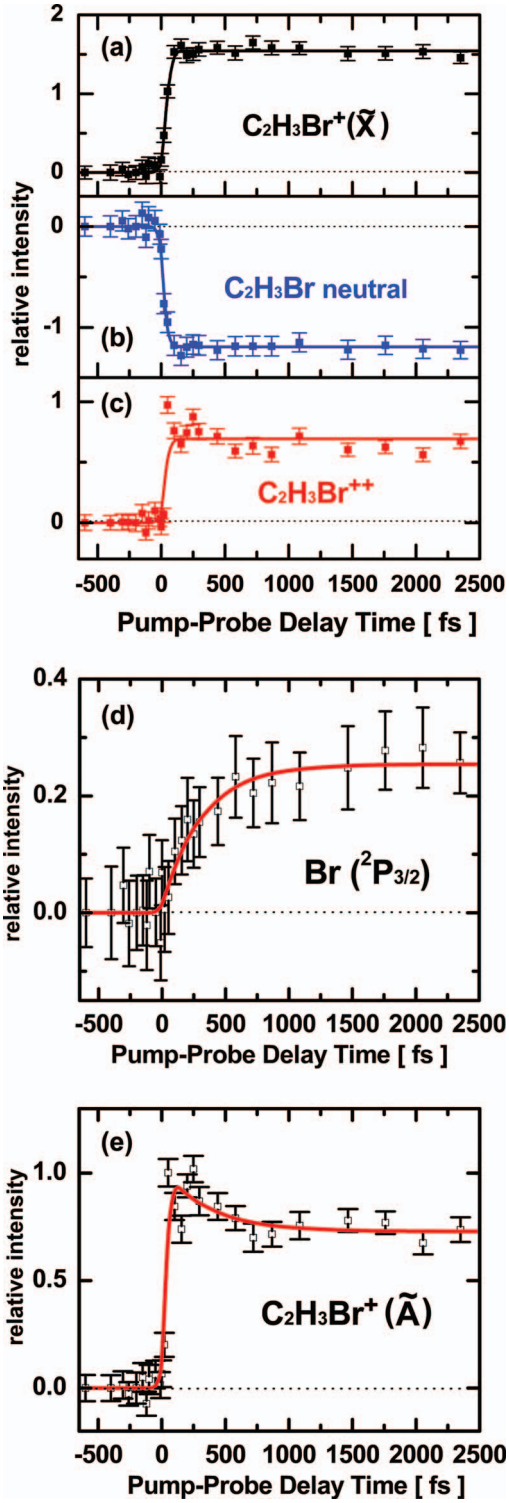

FIG. 9. The pump-probe transient traces for (a) singly charged ions in the ionic $\tilde{X}$ state (black color), (b) the depletion of neutral C_2H_3Br molecules (blue color), and (c) the doubly charged $C_2H_3Br^{++}$ ions (red color). The rising and depletion edges are fit with error functions of FWHMs equal to 65 ± 14 fs and 55 ± 17 fs, respectively. A weighted average IRF of 61 ± 11 fs is derived. A red simulation curve with rising-edge of IRF is plotted over the doubly charged ions to show a promptly production of this transient species. (d) The pump-probe trace of the atomic Br ($^2P_{3/2}$). The red curve represents a free fit of an exponential growth convoluted with an IRF of 61 fs. The resulting exponential rise time is 330 ± 150 fs. (e) The pump-probe transient traces of singly charged ions in the ionic $\tilde{A}$ state. The time trace can be described by the red curve comprising an exponential decay component (330 fs) and constant ion intensity both convoluted with an IRF (61 fs) at rise edge.

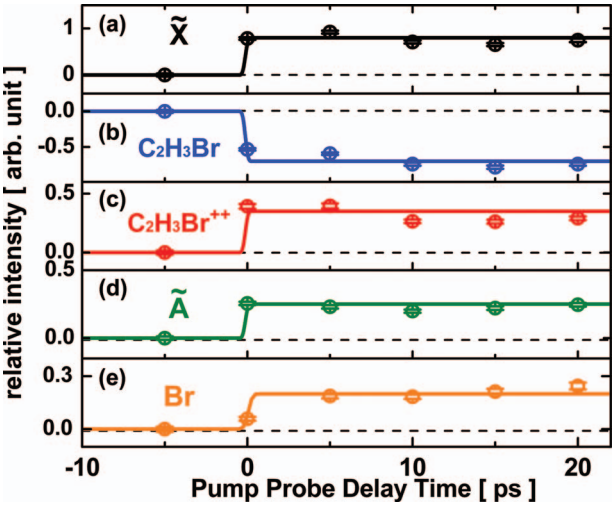

FIG. 10. Transient pump-probe traces of vinyl bromide from −10 ps to 25 ps. Generation of (a) ions in the ionic $\tilde{X}$ state, (b) the depletion of neutral vinyl bromide, (c) the doubly charged $C_2H_3Br^{++}$ ions, (d) singly charged $\tilde{A}$ state ions, and (e) the atomic Br ($^2P_{3/2}$) formation. There is no dynamic change of the transient species after 5 ps. The solid lines represent extended fit curves that describe the pump-probe traces shown in Fig. 9.

mental response functions (IRF), 61 ± 11 fs. In Fig. 9(c), a simulation of the rising edge with an IRF of 61 fs is shown as a red solid line in comparison to the $C_2H_3Br^{++}$ parent ion signal (red markers). This indicates that the doubly charged ions ($C_2H_3Br^{++}$) are generated instantly within the time resolution of this experiment. We are not able to distinguish the subtle difference between sequential and non-sequential double ionization in this experiment. In addition, the small overshoot signal on top of the constant plateau indicates that some dications dissociate into fragment ions within the first few hundred femtoseconds. The majority of dications, however, are long-lived. This will be discussed in Sec. V B.

Figure 9(d) shows the pump-probe trace for the emergence of atomic Br ($^2P_{3/2}$). The trace is fit to a single exponential growth function convoluted with the IRF. The resulting time constant of the single exponential growth is 330 ± 150 fs (red line). Figure 9(e) shows the transient intensity trace for the ionic $\tilde{A}$ state at short pump-probe time delays. The $\tilde{A}$ state signal exhibits a small but noticeable overshoot at early times that decays rapidly toward the asymptotic $\tilde{A}$ state signal level. The limited signal-to-noise ratio of the pump-probe trace prevents a completely free fit using a kinetic model composed of an exponential decay and a constant value. However, the pump-probe trace can be well approximated by a fit curve (red) that represents the sum of an exponential decay with a fixed time constant of 330 fs chosen to match the Br ($^2P_{3/2}$) rise and an instantaneously rising, constant value, both convoluted with the IRF (61 fs). This suggests instantaneous production of $\tilde{A}$ state ions within the time resolution of the experiment that either remains stable within the first few picoseconds or decays into other products within ∼330 fs. The obtained free fit ratio of amplitudes for the decaying vs. constant components is ∼0.37 ± 0.25. Figures 10(a)–10(d) show the pump-probe traces of transient species at time delays ranging from −5 ps to 20 ps. There are no amplitude changes of the transient species from 5 ps to 20 ps, indicating the stability

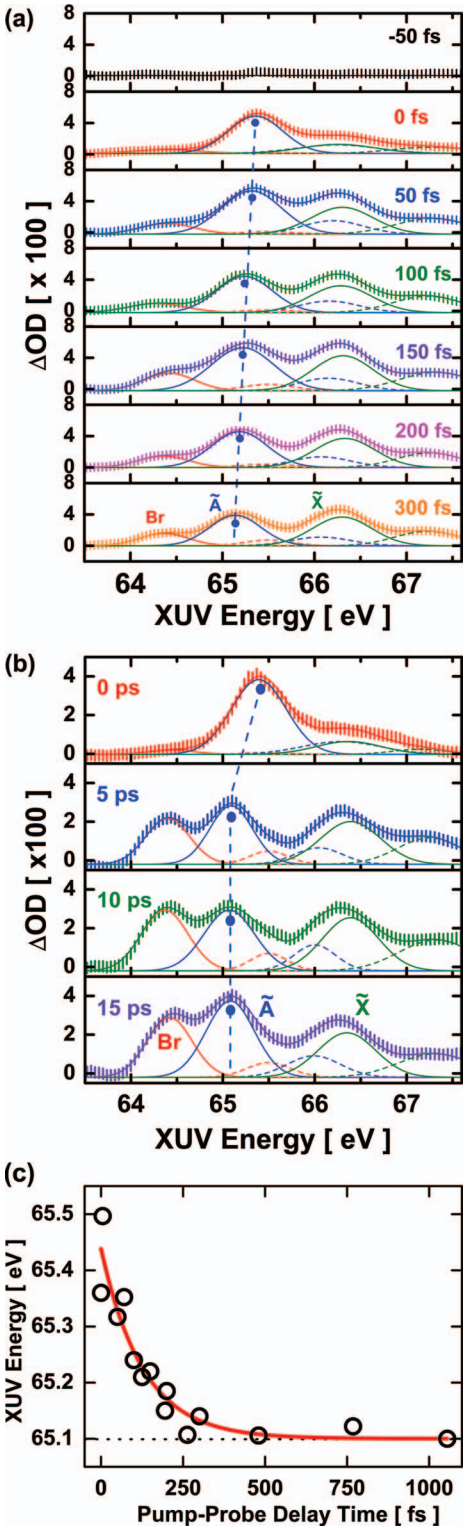

FIG. 11. Transient spectra of vinyl bromide ions at different pump-probe delay windows. (a) From −50 fs to 300 fs (top to bottom). Each spectrum is simultaneously fit with six Gaussian peaks in order to deconvolute the absorption shifts of ions in the ionic $\tilde{A}$ state. (b) From 0 ps to 15 ps (top to bottom). The ions in the $\tilde{A}$ state have presumably reached equilibrium through the dissociation and vibrational relaxation at 5 ps. No changes of absorption energy are observed at delay times from 5 ps to 15 ps (c). The deconvoluted absorption energy of ionic $\tilde{A}$ state versus the pump-probe delay time (black open circles). A clear change of the absorption energy is observed. The red solid line represents a guide for the eye. Note that at time-zero in (a) and (b) the absorption energy of ions in the ionic $\tilde{A}$ state can be subjected to the influence of the NIR field. However, this is limited to the temporal overlap between the XUV and NIR pulses (61 ± 11 fs).

of the singly and doubly charged ions with respect to C–Br bond dissociation in this time window from these states. The solid curves represent extended plots of the fit results shown in Fig. 9 to guide the eye.

Figures 11(a) and 11(b) show a series of transient spectra recorded with pump-probe time delays ranging from −50 fs to 300 fs and 0 ps to 15 ps, respectively. Each spectrum is fit with six Gaussian functions that represent the inner-shell excited spin-orbit components ($3d^{-1}{}_{3/2,5/2}$) for the atomic Br ($^2P_{3/2}$) and the ionic $\tilde{A}$ and $\tilde{X}$ states, as shown in Fig. 7 (Sec. IV A). Free fit parameters are the ion/neutral peak intensities, widths, and positions. The relative absorption strength of each inner-shell excited spin-orbit component is kept the same as those in Fig. 7 while allowing the absolute intensity to float. This systematic deconvolution procedure quantifies the time-dependent energy shift of the ionic $\tilde{A}$ state signal within the first ∼300 fs as noted in Sec. III A (Fig. 4). The time-dependent peak maximum position of the $\tilde{A}$ state signal that results from this series of fits is indicated by small dots in Fig. 11(a); its temporal evolution is shown in Fig. 11(c). The absorption energies of ions in the $\tilde{X}$ state and atomic Br ($^2P_{3/2}$) remain constant. For time delays beyond ∼1 ps, the XUV absorption energies of all transient ions and fragments remain constant (Fig. 11(b)). The red solid line in Fig. 11(c) is derived by an exponential fit of the energy shift and represents a guide for the energy shift of the $\tilde{A}$ state peak. The time constant for the exponential decay is 130 fs. Note that at time zero in Figs. 11(a) and 11(b), the transient ions could be subjected to an AC stark effect that would result in a shift in the absorption energy. However, this effect would be limited to the temporal overlap between the XUV and NIR pulses (IRF 61 fs) and, thus, cannot be responsible for the longer-time dynamics seen here.

C. Correlated densities of transient species in power dependence measurements

Figure 12 displays the areas of the Gaussian peaks that are used to model the transient species versus the NIR peak intensity in Fig. 5. Each spectrum is fit with multiple Gaussian peaks as described in Sec. IV A. The ion signals related

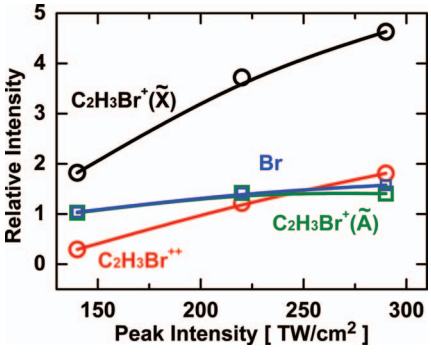

FIG. 12. Area-integrated intensities of transient species versus the NIR peak intensity. The experimental results are shown in open squares and circles. The solid color lines represent a guide for the eye. The intensity correlations are observed between the ionic $\tilde{X}$ state and the doubly charged ions, and between the atomic Br ($^2P_{3/2}$) and the ionic $\tilde{A}$ state.

to the $\tilde{X}$ state and the doubly charged $C_2H_3Br^{++}$ dications increase markedly with increasing NIR peak intensity. However, the signal intensities for the ionic $\tilde{A}$ state and the atomic Br ($^2P_{3/2}$) remain constant. According to Figs. 5 and 12, the depletion of neutral molecules seems to saturate at a NIR peak intensity of 220 TW/cm^2 but the ΔODs of the ionic $\tilde{X}$ state and $C_2H_3Br^{++}$ ions still increase with the NIR peak intensity.

V. DISCUSSION AND THEORETICAL CALCULATIONS

A. Ultrafast relaxation and dissociation dynamics of $C_2H_3Br^+$ ions in the ionic $\tilde{A}$ state

Figures 9(d) and 9(e) demonstrate that the decaying fraction of the $\tilde{A}$ state signal can be characterized by the time constant (330 fs) obtained from the free fit of the emerging atomic Br ($^2P_{3/2}$) signal. This observation suggests that some of the $C_2H_3Br^+$ ions formed in the $\tilde{A}$ state dissociate along the C–Br bond to form atomic Br ($^2P_{3/2}$). In Figs. 11(a) and 11(c), a continuous shift of the XUV absorption peak (∼0.4 eV) associated with the $\tilde{A}$ state of the parent ion is observed. Such an XUV spectral shift has been observed in Br_2 as the result of a vibrational wavepacket produced by SFI.[43] The evolution of the $\tilde{A}$ state absorption energy occurs within the time window during which the C–Br bond breaks. The energy shift of the XUV absorption maximum may, therefore, indicate a vibrational energy redistribution in the $\tilde{A}$ state ions that is followed by the C–Br bond dissociation. The ionic $\tilde{A}$ state has been implicated with respect to the C–Br bond dissociation in a previous study involving single photon ionization.[68]

The relevant energetics for dissociative ionization and ionic dissociation are[68]

$$C_2H_3Br \rightarrow C_2H_3 + Br^+ \quad 15.4\,eV, \tag{1}$$

$$C_2H_3Br \rightarrow {C_2H_3}^+ + Br(^2P_{3/2}) \quad 11.9\,eV, \tag{2}$$

$$C_2H_3Br^+(\tilde{X}) \rightarrow {C_2H_3}^+ + Br(^2P_{3/2}) \quad 2.1\,eV, \tag{3}$$

$$C_2H_3Br^+(\tilde{A}) \rightarrow {C_2H_3}^+ + Br(^2P_{3/2}) \quad 1.0\,eV. \tag{4}$$

Equations (1) and (2) show that DI to Br^+ ions is a considerably higher energy channel than DI to neutral Br($^2P_{3/2}$). Equations (3) and (4) show the energies required for the formation of atomic Br ($^2P_{3/2}$) relative to the minima of the ionic $\tilde{X}$ and $\tilde{A}$ states, respectively.[69–71] The dissociation threshold of the $\tilde{X}$ state is twice as high as that of the $\tilde{A}$ state. Hence, if SFI creates ions in the $\tilde{X}$ and $\tilde{A}$ states with comparable levels of internal excitation, one can envision that some of the $\tilde{A}$ state ions but none or relatively few of the $\tilde{X}$ state ions will have enough energy to dissociate, leading to a depletion of the $\tilde{A}$ state population and a shifting of its XUV electronic band at short pump-probe time delays, as the hotter ions fall apart. However, without a better understanding of the vibrational energy distribution produced by SFI, one cannot say if this simple energetic argument suffices to explain the differences in the temporal behavior of the $\tilde{X}$ and $\tilde{A}$ state signals, or if SFI selectively deposits more internal energy into $\tilde{A}$ state ions than $\tilde{X}$ state ions.

In principle, atomic Br ($^2P_{3/2}$) can be produced from the dissociation of neutral vinyl bromide along the C–Br bond. Such an excitation process would require four NIR photons to reach the neutral excited state at 6.4 eV ($^1\pi\pi^*$).[58] This excited state may cross to a lower energy state that breaks the C–Br bond.[58] The power dependence of both the atomic Br ($^2P_{3/2}$) and the ionic $\tilde{A}$ state yields is strongly saturated (Fig. 12), supporting the picture of strong-field ionization of vinyl bromide leading to C–Br bond dissociation from the ionic $\tilde{A}$ state. The saturation of ion production as a function of NIR peak intensity in the strong-field ionization regime has previously been reported.[72] The strong-field ionization process would ionize neutral vinyl bromide molecules before the C–Br bond dissociation occurs. Therefore, the contribution of atomic Br ($^2P_{3/2}$) from the dissociation of neutral vinyl bromide molecules is unlikely.[34,73] Internal conversion from the ionic $\tilde{A}$ state to the $\tilde{X}$ state accompanying the dissociation of the C–Br bond in the $\tilde{A}$ state is also unlikely. The rise time of the ground state parent ions is 65 ± 14 fs, which does not agree with the slower time constant of atomic Br formation (330 ± 150 fs) and the comparable time constant of the partial $\tilde{A}$ state population decay. The constant intensity of the ground state ions also indicates that dissociation of the C–Br bond in this state is unlikely.

B. Generation and stability of $C_2H_3Br^{++}$ ions

The small overshoot signal at early times in Fig. 9(c) indicates that some hot dications with sufficient internal energy may dissociate into fragments. Figure 10(c), however, shows that nearly all doubly charged $C_2H_3Br^{++}$ ions are long-lived and do not undergo dissociation through Coulomb explosion over time delays ranging up to 20 ps. Metastable dications of unsaturated hydrocarbons with lifetimes on the order of nanoseconds have been observed in several TOF studies.[74,75] According to GAUSSIAN 09 calculations for vinyl bromide, removing two electrons from the HOMO orbital requires the lowest total ionization energy for the generation of the dication (27.2 eV). Under the assumption that the lowest energy state of $C_2H_3Br^{++}$ dications is generated, we perform DFT calculations to estimate the stability of this ion. A theoretical calculation illustrated in Fig. 13 indicates several possible dication dissociation pathways following the dissociative ionization of vinyl bromide. The appearance potentials for three different dissociation channels are given by Eqs. (5)–(7),

$$C_2H_3Br \rightarrow C_2H_3 + Br^{++} \quad 36.8\,eV, \tag{5}$$

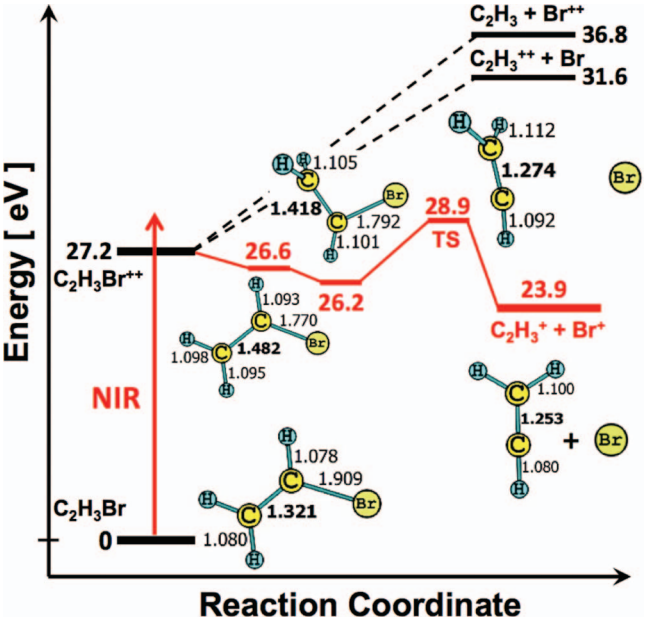

FIG. 13. Dissociative ionization channels of vinyl bromide dications. The dications are generated by ionizing two electrons from the HOMO. The red and black color lines represent the low energetic dissociation and high energetic dissociation channels. The double ionization and dissociative ionization energies are obtained by performing DFT calculations with B3LYP exchange/correlation and 6-311++G (3*d*, 2*p*) basis sets. A transition state is found for $C_2H_3Br^{++} \rightarrow C_2H_3^+ + Br^+$ channel. The dissociation barrier at 28.9 eV supports the possible stability of the $C_2H_3Br^{++}$ parent ions. The numbers on the molecular structures denote the bond distance in Å.

$$C_2H_3Br \rightarrow C_2H_3^{++} + Br \quad 31.6\,eV, \tag{6}$$

$$C_2H_3Br \rightarrow C_2H_3^+ + Br^+ \quad 23.9\,eV. \tag{7}$$

The uneven charge separation channels (Eqs. (5) and (6)) are considerably higher in energy and, thus, much less likely to play a role in the dication dissociation dynamics. Therefore we focus solely on Eq. (7). As shown in Fig. 13, the vertical ionization energy for the generation of $C_2H_3Br^{++}$ dications is 27.2 eV. This energy is higher than that required to produce $C_2H_3^+ + Br^+$ ions. Table II summarizes the dication bond angles and bond lengths for the local minimum at 26.6 eV, ground state dications at 26.2 eV, and transition state structures (28.9 eV) along the dissociation channels according to Eq. (7). The optimized structure for free $C_2H_3^+$ ions is also listed in the table. Right after vertical double ionization within the NIR pulse, the molecular ions elongate along the C–C bond to a local minimum at 26.6 eV. This stretching

TABLE II. Optimized structures parameters for the $C_2H_3Br^{++}$ dications at local minimum (26.6 eV), ground state (26.2 eV), and transition state (28.9 eV). The optimized structure for $C_2H_3^+$ ion is also shown. The bond angle and bond length are in degree and Å, respectively.

$C_2H_3Br^{++} \rightarrow C_2H_3^+ + Br^+$	Local minimum at 26.6 eV	Ground state at 26.2 eV	Transition state at 28.9 eV	$C_2H_3^+$ ground state
r (CBr)	1.770	1.792	3.5	NA
r (CC)	1.482	1.418	1.274	1.253
θ (CCH)	121.12	136.2	170.67	179.99
θ (HCH)	119.49	118.76	116.26	117.33

enables a rotation around the C–C bond toward a structure that has staggered geometry at 26.2 eV. Elimination of the Br^+ ion would proceed through a transition state at 28.9 eV that is marked by a Y-shaped $C_2H_3^+$ radical ion. The 1.7 eV higher energy of this transition state compared to the initial Franck-Condon active dication state may explain the long lifetime of the majority of dications produced by SFI. However, some dications with higher internal energy may dissociate to form fragment ions.

In our measurements, we do not probe dynamics beyond 20 ps, where dissociation of dications into $C_2H_3^+ + Br^+$ ions may occur. This channel has been observed in a previous SFI study[76] that used ion TOF spectroscopy to collect the dissociation products in a nanosecond time window.

VI. CONCLUSIONS AND OUTLOOK

The ultrafast dissociative ionization and relaxation dynamics of vinyl bromide exposed to a strong NIR laser field have been studied with a table-top femtosecond XUV transient absorption setup. The NIR field removes electrons both from the HOMO and HOMO−1 of neutral vinyl bromide (C_2H_3Br), corresponding to the generation of ionic $\tilde{X}$ and $\tilde{A}$ states, respectively. Ions in the $\tilde{X}$ state are long lived with lifetimes longer than 20 ps. Most of the ions in the $\tilde{A}$ state do not dissociate in the time window of 20 ps. However, some ions in the $\tilde{A}$ state, presumably those with high internal energies, appear to dissociate within a few hundred femtoseconds, leading to a decay of the ionic $\tilde{A}$ state population and a dynamic shift of the XUV absorption energy by ∼0.4 eV. The time scales for the decay of the $\tilde{A}$ state ions and their dynamic energy shift are close to or smaller than the time constant for the atomic Br ($^2P_{3/2}$) emergence (330 ± 150 fs), suggesting that the C–Br bond dissociation occurs from the ionic $\tilde{A}$ state.

NIR power dependence measurements indicate a correlation between the time-dependent signals associated with $\tilde{A}$ state ions and atomic Br ($^2P_{3/2}$) fragments, supporting the formation of free atomic Br ($^2P_{3/2}$) from the $\tilde{A}$ state. Electronic structure calculations suggest that an energy barrier along the dissociative reaction coordinate of $C_2H_3Br^{++}$ to form $C_2H_3^+ + Br^+$ may prevent direct dissociation of the dication, indicating the production of stable ions upon ionizing two electrons from the HOMO orbital.

The current study demonstrates that a tabletop femtosecond XUV light source can be used to probe the ultrafast dissociation dynamics of ions by monitoring changes in the XUV absorption strength and energy. The dynamics of vinyl bromide molecular ions with a broad internal energy distribution have been investigated. In future studies, this method will be applied to molecules excited by one-photon excitation processes and with known internal energies. Dynamics around conical intersections, internal conversion, and ring-opening dynamics of excited polyatomic molecules will be explored with femtosecond time resolution and element specificity.

ACKNOWLEDGMENTS

We thank Scott Sayres and Chih-Yuan Lin for discussions of strong-field ionization of polyatomic molecules and spin-orbit coupling of valence orbitals. We appreciate the help of Camila Bacellar, Neil Cole-Filipiak, and Alex Shreve with respect to the theoretical calculations using the GAUSSIAN 09 program package. This work was supported by the Director, Office of Science, Office of Basic Energy Sciences, Chemical Sciences, Geosciences, and Biosciences Division of the U.S. Department of Energy under Contract No. DE-AC02-05CH11231. S.R.L. acknowledges the support of a National Security Science and Engineering Faculty Fellowship. M.-F. Lin also expresses gratitude for a fellowship from the Ministry of Education, Taiwan, Republic of China.

[1] G. Vall-llosera, B. Gao, A. Kivimaki, M. Coreno, J. A. Ruiz, M. d. Simone, H. Agren, and E. Rachlew, J. Chem. Phys. **128**, 044316 (2008).
[2] B. X. Yang and J. Kirz, Phys. Rev. B **36**, 1361 (1987).
[3] P. Wernet, J. Phys. Conf. Ser. **190**, 012055 (2009).
[4] H. Oji, R. Mitsumoto, E. Ito, H. Ishii, Y. Ouchi, K. Seki, T. Yokoyama, T. Ohta, and N. Kosugi, J. Chem. Phys. **109**, 10409 (1998).
[5] K. Kaznacheyev, A. Osanna, C. Jacobsen, O. Plashkevych, O. Vahtras, H. Agren, V. Carravetta, and A. P. Hitchcock, J. Phys. Chem. A **106**, 3153 (2002).
[6] F. A. Lima, C. J. Milne, D. C. V. Amarasinghe, M. H. Rittmann-Frank, R. M. v. d. Veen, M. Reinhard, V.-T. Pham, S. Karlsson, S. L. Johnson, D. Grolimund, C. Borca, T. Huthwelker, M. Janousch, F. v. Mourik, R. Abela, and M. Chergui, Rev. Sci. Instrum. **82**, 063111 (2011).
[7] A. M. March, A. Stickrath, G. Doumy, E. P. Kanter, B. Krassig, S. H. Southworth, K. Attenkofer, C. A. Kurtz, L. X. Chen, and L. Young, Rev. Sci. Instrum. **82**, 073110 (2011).
[8] Z.-H. Loh, M. Khalil, R. E. Correa, and S. R. Leone, Rev. Sci. Instrum. **79**, 073101 (2008).
[9] M. Saes, F. v. Mourik, W. Gawelda, M. Kaiser, M. Chergui, C. Bressler, D. Grolimund, R. Abela, T. E. Glover, P. A. Heimann, R. W. Schoenlein, S. L. Johnson, A. M. Lindenberg, and R. W. Falcone, Rev. Sci. Instrum. **75**, 24 (2004).
[10] L. X. Chen, W. J. H. Jäger, G. Jennings, D. J. Gosztola, A. Munkholm, and J. P. Hessler, Science **292**, 262 (2001).
[11] C. J. Milne, V.-T. Pham, W. Gawelda, R. M. v. d. Veen, A. E. Nahhas, S. L. Johnson, P. Beaud, G. Ingold, F. Lima, D. A. Vithanage, M. Benfatto, D. Grolimund, C. Borca, M. Kaiser, A. Hauser, R. Abela, C. Bressler, and M. Chergui, J. Phys. Conf. Ser. **190**, 012052 (2009).
[12] C. Bressler and M. Chergui, Chem. Rev. **104**, 1781 (2004).
[13] C. Bressler and M. Chergui, Annu. Rev. Phys. Chem. **61**, 263 (2010).
[14] E. Gagnon, P. Ranitovic, X.-M. Tong, C. L. Cocke, M. M. Murnane, H. C. Kapteyn, and A. S. Sandhu, Science **317**, 1374 (2007).
[15] R. W. Schoenlein, S. Chattopadhyay, H. H. W. Chong, T. E. Glover, P. A. Heimann, C. V. Shank, A. A. Zholents, and M. S. Zolotorev, Science **287**, 2237 (2000).
[16] T. Pfeifer, C. Spielmann, and G. Gerber, Rep. Prog. Phys. **69**, 443 (2006).
[17] E. J. Takahashi, Y. Nabekawa, H. Mashiko, H. Hasegawa, A. Suda, and K. Midorikawa, IEEE J. Sel. Top. Quant. **10**, 1315 (2004).
[18] L. X. Chen, Annu. Rev. Phys. Chem. **56**, 221 (2005).
[19] L. X. Chen, Angew. Chem., Int. Ed. **43**, 2886 (2004).
[20] P. Emma, Nat. Photon. **4**, 641 (2010).
[21] T. Popmintchev, M.-C. Chen, P. Arpin, M. M. Murnane, and H. C. Kapteyn, Nat. Photon. **4**, 822 (2010).
[22] T. Popmintchev, M.-C. Chen, A. Bahabad, M. Gerrity, P. Sidorenko, O. Cohen, I. P. Christov, M. M. Murnane, and H. C. Kapteyn, Proc. Natl. Acad. Sci. U.S.A. **106**, 10516 (2009).
[23] O. Kornilov, C. C. Wang, O. Bünermann, A. T. Healy, M. Leonard, C. Peng, S. R. Leone, D. M. Neumark, and O. Gessner, J. Phys. Chem. A **114**, 1437 (2010).
[24] H. Cho, M. L. Strader, K. Hong, L. Jamula, E. M. Gullikson, T. K. Kim, F. M. F. de Groot, J. K. McCusker, R. W. Schoenlein, and N. Huse, Faraday Discuss. **157**, 463 (2012).
[25] N. Huse, H. Cho, K. Hong, L. Jamula, F. M. F. de Groot, T. K. Kim, J. K. McCusker, and R. W. Schoenlein, J. Phys. Chem. Lett. **2**, 880 (2011).
[26] E. Goulielmakis, Z. H. Loh, A. Wirth, R. Santra, N. Rohringer, V. S. Yakovlev, S. Zherebtsov, T. Pfeifer, A. M. Azzeer, M. F. Kling, S. R. Leone, and F. Krausz, Nature (London) **466**, 739 (2010).
[27] J. Breidbach and L. S. Cederbaum, J. Chem. Phys. **118**, 3983 (2003).
[28] I. V. Schweigert and S. Mukamel, Phys. Rev. A **76**, 012504 (2007).

[29]A. I. Kuleff and L. S. Cederbaum, Phys. Rev. Lett. **98**, 083201 (2007).
[30]M. Drescher, M. Hentschel, R. Kienberger, M. Uiberacker, V. Yakovlev, A. Scrinzi, T. Westerwalbesloh, U. Kleineberg, U. Heinzmann, and F. Krausz, Nature (London) **419**, 803 (2002).
[31]Z. H. Loh, C. H. Greene, and S. R. Leone, Chem. Phys. **350**, 7 (2008).
[32]Z.-H. Loh, M. Khalil, R. E. Correa, R. Santra, C. Buth, and S. R. Leone, Phys. Rev. Lett. **98**, 143601 (2007).
[33]M.-F. Lin, A. N. Pfeiffer, D. M. Neumark, S. R. Leone, and O. Gessner, J. Chem. Phys. **137**, 244305 (2012).
[34]Z.-H. Loh and S. R. Leone, J. Chem. Phys. **128**, 204302 (2008).
[35]P. Ranitovic, X. M. Tong, C. W. Hogle, X. Zhou, Y. Liu, N. Toshima, M. M. Murnane, and H. C. Kapteyn, Phys. Rev. Lett. **106**, 053002 (2011).
[36]P. Ranitovic, X. M. Tong, C. W. Hogle, X. Zhou, Y. Liu, N. Toshima, M. M. Murnane, and H. C. Kapteyn, Phys. Rev. Lett. **106**, 193008 (2011).
[37]X. Feng, S. Gilbertson, H. Mashiko, H. Wang, S. D. Khan, M. Chini, Y. Wu, K. Zhao, and Z. Chang, Phys. Rev. Lett. **103**, 183901 (2009).
[38]H. Wang, M. Chini, S. Chen, C.-H. Zhang, F. He, Y. Cheng, Y. Wu, U. Thumm, and Z. Chang, Phys. Rev. Lett. **105**, 143002 (2010).
[39]M. Chini, B. Zhao, H. Wang, Y. Cheng, S. X. Hu, and Z. Chang, Phys. Rev. Lett. **109**, 073601 (2012).
[40]M. Schultze, M. Fieß, N. Karpowicz, J. Gagnon, M. Korbman, M. Hofstetter, S. Neppl, A. L. Cavalieri, Y. Komninos, T. Mercouris, C. A. Nicolaides, R. Pazourek, S. Nagele, J. Feist, J. Burgdörfer, A. M. Azzeer, R. Ernstorfer, R. Kienberger, U. Kleineberg, E. Goulielmakis, F. Krausz, and V. S. Yakovlev, Science **328**, 1658 (2010).
[41]R. Kienberger, M. Hentschel, M. Uiberacker, C. Spielmann, M. Kitzler, A. Scrinzi, M. Wieland, T. Westerwalbesloh, U. Kleineberg, U. Heinzmann, M. Drescher, and F. Krausz, Science **297**, 1144 (2002).
[42]E. Goulielmakis, V. S. Yakovlev, A. L. Cavalieri, M. Uiberacker, V. Pervak, A. Apolonski, R. Kienberger, U. Kleineberg, and F. Krausz, Science **317**, 769 (2007).
[43]E. R. Hosler and S. R. Leone, Phys. Rev. A **88**, 023420 (2013).
[44]A. E. Boguslavskiy, J. Mikosch, A. Gijsbertsen, M. Spanner, S. Patchkovskii, N. Gador, M. J. J. Vrakking, and A. Stolow, Science **335**, 1336 (2012).
[45]D. A. Telnov and S.-I. Chu, Phys. Rev. A **80**, 043412 (2009).
[46]X. Chu and S.-I. Chu, Phys. Rev. A **70**, 061402 (2004).
[47]A. N. Markevitch, S. M. Smith, D. A. Romanov, H. Bernhard Schlegel, M. Y. Ivanov, and R. J. Levis, Phys. Rev. A **68**, 011402 (2003).
[48]M. Lezius, V. Blanchet, M. Y. Ivanov, and A. Stolow, J. Chem. Phys. **117**, 1575 (2002).
[49]G. C. King, M. Tronc, F. H. Read, and R. C. Bradford, J. Phys. B: At., Mol. Opt. Phys. **10**, 2479 (1977).
[50]M. Sano, Y. Itoh, T. Koizumi, T. M. Kojima, S. D. Kravis, M. Oura, T. Sekioka, N. Watanabe, Y. Awaya, and F. Koike, J. Phys. B: At., Mol. Opt. Phys. **29**, 5305 (1996).
[51]P. Andersen, T. Andersen, F. Folkmann, V. K. Ivanov, H. Kjeldsen, and J. B. West, J. Phys. B: At., Mol. Opt. Phys. **34**, 2009 (2001).
[52]M. J. Frisch, G. W. Trucks, H. B. Schlegel *et al.*, GAUSSIAN 09, Revision C.01, Gaussian, Inc., Wallingford, CT, 2010.
[53]B. Brehm, U. Fröbe, and H. P. Neitzke, Int. J. Mass Spectrom. Ion Processes **57**, 91 (1984).
[54]K. H. Sze, C. E. Brion, and A. Katrib, Chem. Phys. **132**, 271 (1989).
[55]M. Lee and M. S. Kim, J. Chem. Phys. **126**, 154317 (2007).
[56]A. Hoxha, R. Locht, B. Leyh, D. Dehareng, K. Hottmann, and H. Baumgartel, Chem. Phys. **256**, 239 (2000).
[57]A. Hoxha, R. Locht, B. Leyh, D. Dehareng, K. Hottmann, H. W. Jochims, and H. Baumgartel, Chem. Phys. **260**, 237 (2000).
[58]K. H. Sze, C. E. Brion, A. Katrib, and B. Elissa, Chem. Phys. **137**, 369 (1989).
[59]J. Johnson, J. N. Cutler, G. M. Bancroft, Y. F. Hu, and K. H. Tan, J. Phys. B: At., Mol. Opt. Phys. **30**, 4899 (1997).
[60]R. N. Dixon and H. W. Kroto, Trans. Faraday Soc. **59**, 1484 (1963).
[61]J. Stöhr, *NEXAFS Spectroscopy* (Springer, 1996), p. 72.
[62]A. Cummings and G. O'Sullivan, Phys. Rev. A **54**, 323 (1996).
[63]J. Schirmer, M. Braunstein, M.-T. Lee, and V. McKoy, *VUV and Soft X-Ray Photoionization* (Plenum, New York, 1996), pp. 105–133.
[64]A. Stolow, Annu. Rev. Phys. Chem. **54**, 89 (2003).
[65]M. Mazzoni and M. Pettini, Phys. Lett. A **85**, 331 (1981).
[66]B. E. Miller and T. Baer, Chem. Phys. **85**, 39 (1984).
[67]A. F. Lago and T. Baer, J. Phys. Chem. A **110**, 3036 (2006).
[68]A. Hoxha, S. Y. Yu, R. Locht, H. W. Jochims, and B. Leyh, Chem. Phys. **379**, 99 (2011).
[69]M. Lee and M. S. Kim, J. Chem. Phys. **123**, 174310 (2005).
[70]Y. Y. Youn, J. C. Choe, and M. S. Kim, J. Am. Soc. Mass Spectrom. **14**, 110 (2003).
[71]X. M. Qian, K. C. Lau, and C. Y. Ng, J. Chem. Phys. **120**, 11031 (2004).
[72]M. Tanaka, M. Murakami, T. Yatsuhashi, and N. Nakashima, J. Chem. Phys. **127**, 104314 (2007).
[73]J. H. Posthumus, Rep. Prog. Phys. **67**, 623 (2004).
[74]S. M. Sharifi, A. Talebpour, and S. L. Chin, J. Phys. B: At., Mol. Opt. Phys. **40**, F259 (2007).
[75]S. M. Sharifi, A. Talebpour, and S. L. Chin, J. Atom. Mol. Phys. **2009**, 573020 (2009).
[76]M. Castillejo, M. Martín, R. de Nalda, S. Couris, and E. Koudoumas, J. Phys. Chem. A **106**, 2838 (2002).